Journal of Dynamic Behavior of Materials
https://doi.org/10.1007/s40870-020-00273-5

S.I. : IMPACT MATTERS: K.T. RAMESH'S 60TH BIRTHDAY

Thermo-Mechanical Response of an Additively Manufactured Energetic Material Simulant to Dynamic Loading

A. Keyhani[1] · M. Zhou[1,2]

Received: 16 March 2020 / Accepted: 17 September 2020

Abstract
The mesoscale thermo-mechanical behavior of an additively manufactured energetic material (AMEM) simulant under dynamic loading is studied. The material is unidirectionally printed using direct ink writing (DIW) of a high solid-loaded photopolymer and cured under ultraviolet (UV) light exposure. Experiments and multi-physics computations are performed to relate localized deformation, dissipation mechanisms, and temperature rises to the print structure. Simultaneous high-speed visible light and infrared imaging is used to obtain deformation and temperature fields over the same area of samples with micrometer spatial and microsecond temporal resolutions. Loading along different directions relative to the print structure of the material is achieved using a split-Hopkinson pressure bar (SHPB) or Kolsky bar at the average strain rate of ~ 310 s^{-1}. Shear banding and shear failure are observed. Simulations accounting for the geometry and print structure of the samples are performed. The microstructural heterogeneities are found to significantly affect the orientation-dependent deformation, damage, and heating, with the damage and heating most pronounced when the loading direction and print orientation are non-collinear. The heating is attributed to both constituent inelastic dissipation and internal friction. Depending upon the strain rate level and the loading orientation, the contribution of frictional dissipation to the overall heating is 0.9–4.5%. Despite this relatively low fraction in the overall heating, friction is localized at fracture sites and plays an important role in the development of local temperature spikes called hotspots which are of great interest for energetic materials.

Keywords Additively manufactured energetic material (AMEM) · Split-Hopkinson pressure bar (SHPB) · High-speed optical and infrared imaging · Digital image correlation (DIC) · Multi-physics finite element simulation

Introduction

The geometric flexibility provided by additive manufacturing (AM) or 3D-printing opens new avenues for functionally tailoring materials for specific applications. As a result, AM has been widely used to produce a wide range of materials such as metals [1, 2], polymers [3], and energetic materials (EM) [4, 5]. Several AM techniques have been used for EM including electrospray deposition (ESD) [6–8] and direct ink writing (DIW) [9–12]. AM processes result in embedding inherent heterogeneities that can lead to poor mechanical properties [13, 14] and different mechanical behaviors in different directions and regions [15, 16]. Defects, microstructure heterogeneities, and anisotropy can significantly affect the behavior of additively manufactured energetic material (AMEMs) as well [17, 18]. Since heterogeneities have dominant effects on the energy dissipation, hotspots formation [19], and chemical reactions [20, 21] in EM, it is necessary to systematically quantify the mesoscale thermo-mechanical response of AMEMs under dynamic loading in order to tailor these materials for applications, improve performance, and minimize uncertainties.

Experimental analyses of the mesoscale thermo-mechanical response of heterogeneous materials at high spatial and temporal resolutions is challenging. Concurrent multi-physics measurements are rare or near non-existent. Most studies involve either mechanical deformation or thermal response alone [21–23] or the two separately. High-speed visible light (VL) cameras and infrared (IR) thermal detectors have been used to study

✉ M. Zhou
min.zhou@gatech.edu

[1] The George W. Woodruff School of Mechanical Engineering, Georgia Institute of Technology, Atlanta, GA 30332-0405, USA

[2] School of Materials Science and Engineering, Georgia Institute of Technology, Atlanta, GA 30332-0405, USA

Published online: 30 September 2020

thermo-mechanical responses with low spatial resolutions [24–27]. Recently, high-speed IR cameras provide the opportunity to measure temperature fields with unprecedented spatial and temporal resolutions. Using a beam-splitter along with developing a custom-designed lens assembly, Keyhani et al. integrated a high-speed VL camera and a high-speed IR camera [28]. This technique enables coupled recording of the temperature field and the deformation field with micrometer spatial and microsecond temporal resolutions. Here, we use this technique to study the coupled thermal-mechanical behavior of an AMEM simulant.

Unidirectionally printed materials show overall transversely isotropic behavior with the print (filament) direction as the anisotropic axis. In addition, these materials show orientation-dependent failure behavior. Hong et. al tested UV-cured AM photopolymers and reported that the tensile toughness level parallel to the filaments is approximately two times higher than the toughness level perpendicular to the filaments [29]. Therefore, it is necessary to account for anisotropic failure in modeling of AM photopolymers. Based on isotropic hyperelastic and viscoplastic models for polymers [30, 31], Zhang and To proposed a transversely isotropic continuum model for additively manufactured photopolymers [32]. This model applies to the macro-scale behavior of AM photopolymers. However, to understand meso-scale thermo-mechanical response of AMEMs, it is necessary to explicitly account for microstructure morphology and heterogeneities at lower size scales.

The focus here is the mesoscale thermo-mechanical responses under impact loading of a high solid-loaded photopolymer manufactured using the DIW process and cured with UV-light. The material mimics the attributes of some AMEMs. Samples are extracted from a single DIW block and subjected to loading along four different directions. The experiments are performed in a SHPB or Kolsky bar apparatus at the average strain rate of ~ 310 s^{-1}, with the recently developed novel capability for simultaneous measurement of the temperature and deformation fields [28]. The technique involves the use of digital image correlation (DIC) for displacement and strain distribution quantification [33]. The deformation and temperature fields are coordinated to obtain understanding of the deformation, failure, and heating mechanisms in the material at the mesoscale. To quantify the complex physics observed in the experiments and their interplays, finite element simulations are performed accounting for the geometry and microstructure morphology of the samples used in the experiments. The simulations account for finite-strain inelastic deformation, arbitrary crack initiation and propagation, contact and friction at crack surfaces, inelastic and frictional heat generation, and heat conduction. Most material constitutive parameters are obtained from independent experiments or determined using experimental data in the literature.

Technical Approach

Material and Microstructure

The photopolymer composite used in the DIW AM and UV-light curing processes has a solid particulate volume fraction of 74%. The particulate population includes organic and inorganic materials. These printed blocks are approximately $37.8 \times 54.5 \times 13.3$ mm in size. The samples are extracted from these blocks using a diamond saw (Crystal Systems Corporation Model CU-02). Figure 1 shows the external structure of one such a material block. The tomographic images of three sections of the block show internal defects in the forms of voids and debonding sites. Figure 2a shows a three-dimensional view of the voids in this block. The overall volume fraction of voids in the material block is 2%. The size and shape of the voids are characterized using the actual volume and the bounding box of each void. The shapes of two such voids are shown in Fig. 2b. Figure 2c shows the density distributions of the three linear dimensions of the bounding boxes in the x, y, and z directions. The density distributions of the aspect ratios are shown in Fig. 2d. The defects are elongated in the y (print or filament) direction and are relatively flattened in the z (build) direction. The mechanical properties at the primary orientations are obtained from quasi-static tests and listed in Table 1.

Integrated High-speed Visible Light and Infrared Imaging System

Figure 3 illustrates the overall experimental setup for dynamic loading and coupled spatially and temporally resolved recording of the deformation and temperature fields [28]. Dynamic compression of the samples is achieved using a split-Hopkinson pressure bar (SHPB) with a load pulse duration of 0.2 ms and an average strain rate of ~ 310 s^{-1}. To capture the transient deformation and temperature fields over the same microstructure area of a sample with micrometer spatial and microsecond temporal resolutions, a high-speed visible light (VL) imaging camera and a high-speed infrared (IR) imaging camera are used. The two cameras capture the VL and IR parts of the emission spectrum from the sample, respectively. To separate these two parts, a dichroic beam splitter is used, as shown in Fig. 3b. The beam splitter reflects VL and transmits IR emissions at an efficiency of 85%. Both cameras image at normal incidence to the sample service, because the beam splitter is at 45° relative to the sample surface. To correct distortions in the transmitted IR image,

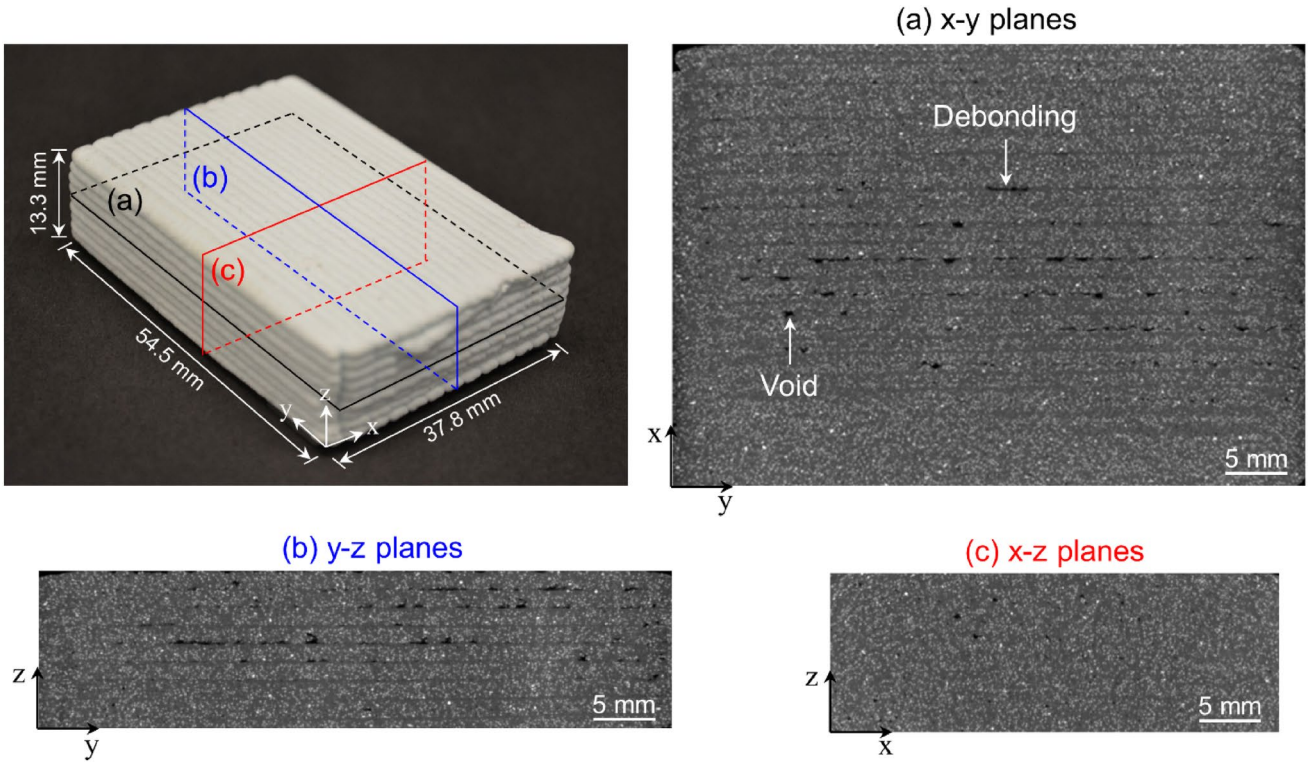

Fig. 1 External structure of a material block and the tomographic images of three sections of the material block. The tomographic images show the internal defects including voids and debonding sites

a custom-designed distortion correction lens assembly is used (Fig. 3b). The IR camera is calibrated in the same optical setting of the actual experiments. The reflected VL image is recorded by the VL camera with a microscope lens. To coordinate the VL and IR images, the cameras are synchronized in time and space. Details of the setup and procedure can be found in reference [28]. The VL images are recorded at a temporal resolution of 10 µs, a spatial resolution of 13.6 µm, and a field of view (FOV) of 7.0 × 4.4 mm. The IR images are captured at a temporal resolution of 300 µs, a spatial resolution of 11.4 µm, and a FOV of 2.2 × 2.2 mm [shown in Fig. 3(c)].

The samples are compressed without lateral confinement. Loading along 4 sample orientations relative to the AM print direction is considered. The 4 loading orientations are along the x direction, y (print or filament) direction, z (build) direction, and xy-diagonal direction. For this purpose, the samples are cut from the AM blocks accordingly at an overall size of 5 × 5 × 5 mm, as illustrated in Fig. 4. The VL and IR FOVs are illustrated. The experiments are carried out at ambient temperatures and humidity levels of 23.3 ± 1.8 °C and 44.6 ± 2.1 %, respectively.

Digital Image Correlation (DIC) Analysis of Deformation Fields

To quantify the strain distributions in the samples, digital image correlation (DIC) analyses are performed using the open-source Ncorr package [34]. To provide characteristic patterns for the image correlation, the surfaces of the samples are sparsely sprayed with the black paint. The speckle patterns sprayed on the samples are shown in Fig. 5a. The probability density distributions of speckle dimensions are shown in Fig. 5b. The proper size of 3–6 pixels is achieved for speckles [35]. Higher densities of speckles can lead to higher resolutions for deformation fields, but cover higher fractions of sample surfaces resulting in more interference with the temperature measurement. Here, the densities of speckles are limited to 16.5 ± 1.4% (Fig. 5c) to maintain a proper tradeoff between the deformation resolution and the temperature measurement accuracy.

To estimate the errors in the DIC analyses, the displacement and strain fields readings associated with known rigid translations of the samples are calculated. In this scenario, the samples are translated in the loading direction

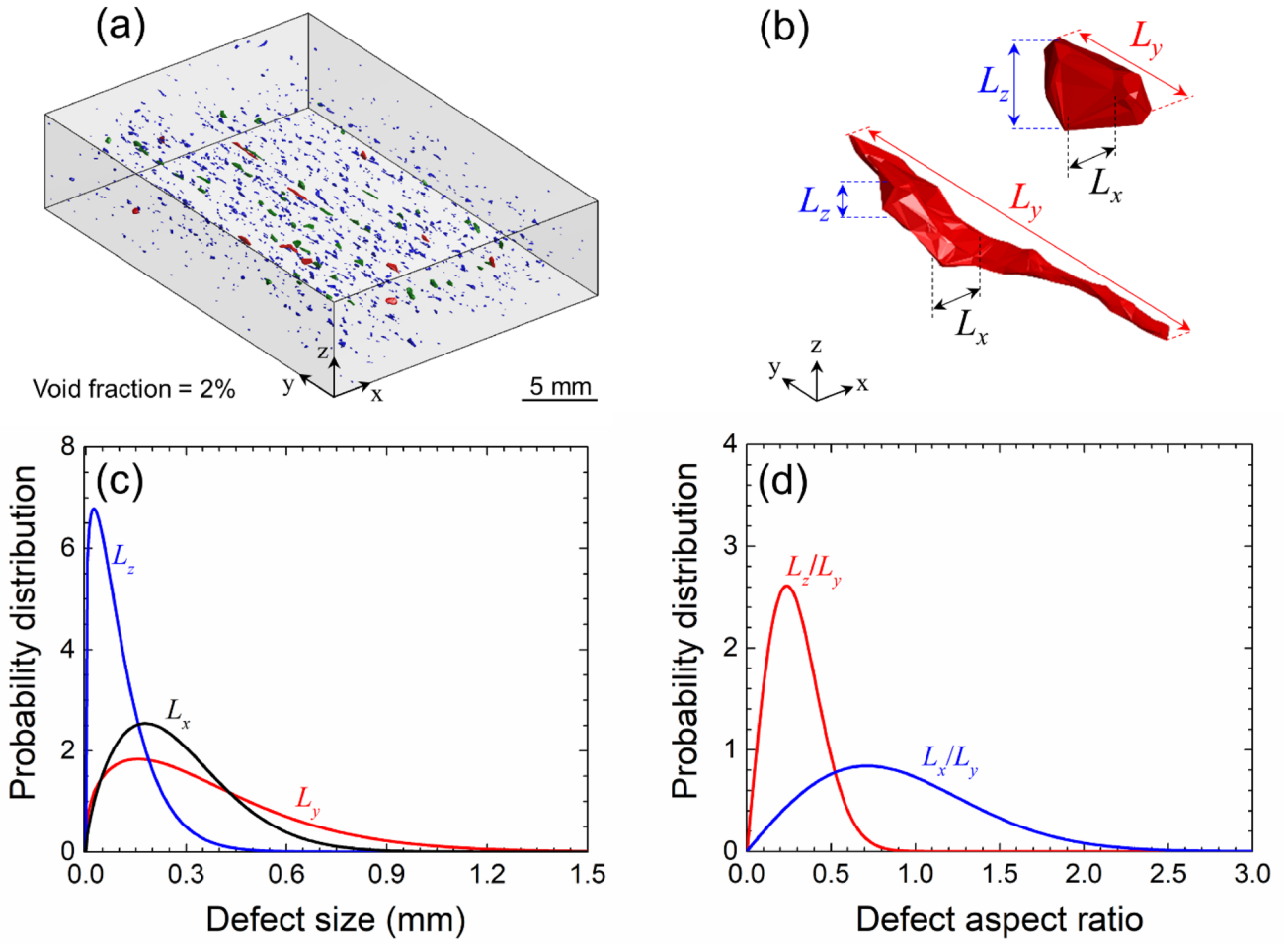

Fig. 2 **a** The distribution of voids in a 3D-printed photopolymer-solid particle composite block, **b** the shapes of two voids, **c** probability density distributions of defect sizes in the x, y, and z directions, and **d** probability density distributions of defect aspect ratios. The overall void fraction in the material is 2%

Table 1 Mechanical properties of the AMEM simulant in different orientations

Loading orientation	E(GPa)	σ_c(MPa)	ε_c(%)
Along filaments (y)	2.54 ± 0.05	23.95 ± 4.50	1.15 ± 0.18
Perpendicular to filaments (x and z)	0.97 ± 0.19	21.64 ± 3.02	2.57 ± 0.76

E is the Young's modulus, σ_c is the yield stress in compression, and ε_c is the yield strain in compression

(x-direction) without deformation. Under ideal conditions, the DIC analyses should yield uniform displacement field and zero strain. Any deviation from the applied displacement and resulting strain field provide a measure for the error in the DIC analyses and associated experimental setup. Figures 6a and b show the probability density distributions of error in the displacement along the loading or x-direction at $x = 2$ and 4 mm, respectively. Three subset sizes of 30, 50, and 70 pixels are used. Here, the selection of subset sizes smaller than 30 pixels results in incomplete and noisy strain fields. For all selected subset sizes, the maximum displacement error is ~ 9 µm, which is smaller than the pixel size of 13.6 µm. Figure 6c and d show the error in the longitudinal strain, the maximum is 7×10^{-3}, associated with the smallest subset size (30 pixels). Using the subset size of 30 pixels, Figs. 7a and b show the probability distributions of displacement error along the loading direction in the four samples. Figures 7c and d show the probability distributions of the error in the longitudinal strain in the four samples. The maximum error in the longitudinal strain calculations is 10^{-2}. In the analyses, a subset size of 30 pixels is used, with the uncertainty levels in the displacement and strain being 9 µm and 1%, respectively.

Thermo-mechanical Computational Simulations

The experiments capture deformation modes and corresponding temperature signatures in the AMEM simulant.

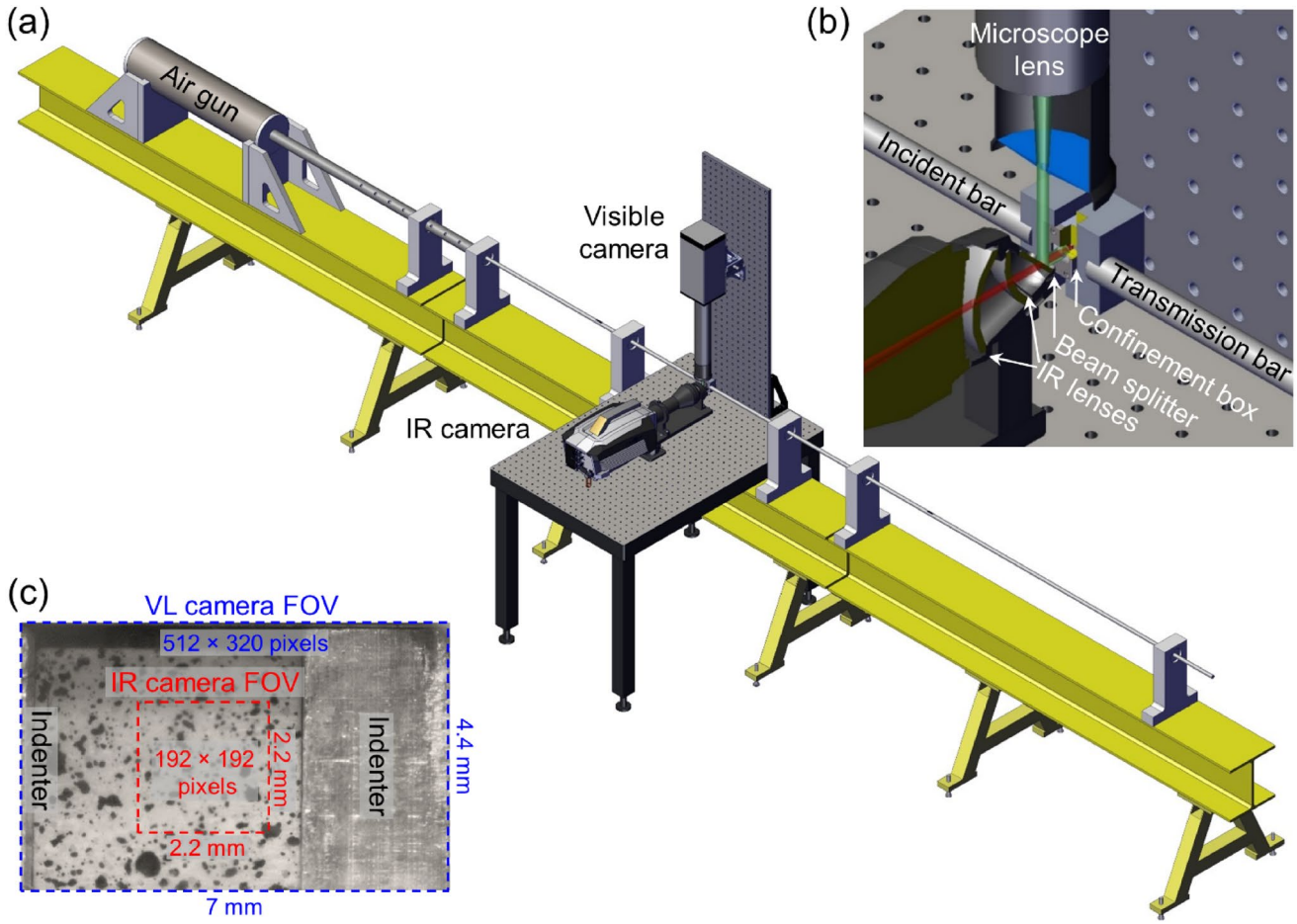

Fig. 3 Experimental setup for dynamic loading and simultaneous high-speed infrared (IR) and visible (VL) imaging of microscale temperature and deformation fields; **a** configuration of the split-Hopkinson bar apparatus and visible and infrared cameras, **b** relative positions of the confinement box, the dichroic beam splitter, the visible microscope lens, and the infrared lens assembly, and **c** relative positions of visible and infrared fields of view

However, the effects of microstructural attributes and frictional and inelastic dissipation cannot be quantified experimentally due to limitations of available diagnostics. Therefore, we also perform experimentally-informed finite element simulations to gain the quantification.

Microstructures are generated based on scanned images of the morphology of the 3D-printed material block. Material constitutive parameters are determined based on independent experiments or data reported in the literature. The Young's modulus and the yield strength are measured through quasi-static tests. The equation of state (EOS) is obtained through our recent x-ray phase contrast imaging (XPCI) experiments on this material [36]. The damage and thermal parameters are approximated to match the results of simultaneous high-speed optical and infrared images. Here, we assume that the filaments are homogenous elastic-plastic materials. The inhomogeneities in the material are modeled through material property variations from one filament to another. Since the defects are mainly located at the inter-filament sites, they are implicitly modeled through reduction in the mass density and degradation in the mechanical properties at the inter-filament sites [see Fig. 4b]. A critical plastic strain criterion determines the initiation and propagation of shear failure. The onset of damage at the two-filament junctions and three-filament junctions are approximated to be two-thirds and one-third of the filaments, respectively [29]. The material property sets are listed in Table 2 and color-coded through this paper.

The experiments suggest that friction can contribute significantly to the heating in the material, as the highest temperatures measured are inside shear bands where shear failure occurs. Therefore, it is important to account for frictional dissipation as well as inelastic dissipation in the simulations. To do this, we use a Lagrangian framework that explicitly tracks interfaces resulting from material failure, interfacial frictional sliding, and consequent frictional heating. The simulations also account for finite-strain elastic-plastic deformation, strain-rate effect, inelastic heating, and heat conduction. To prevent

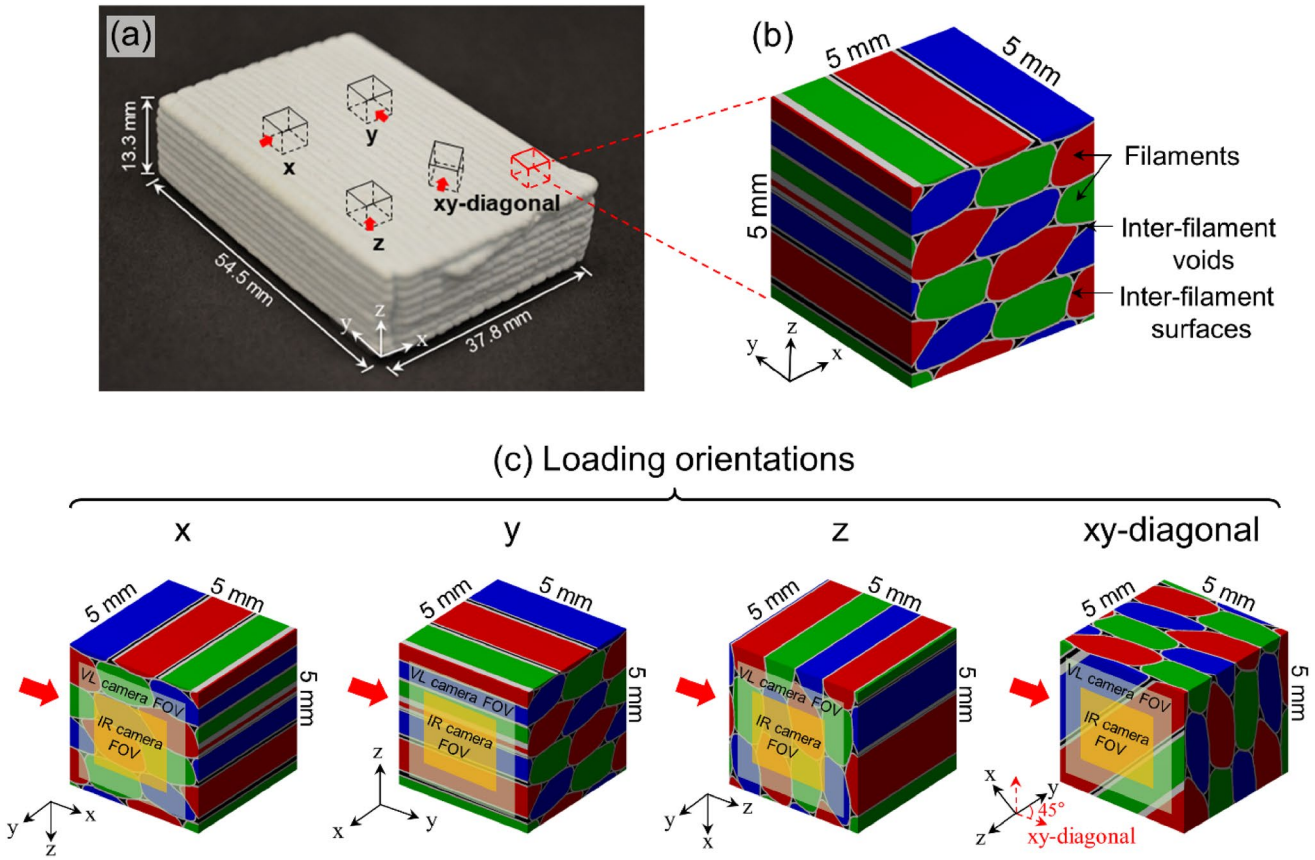

Fig. 4 Illustration of loading directions with respect to the print structure. The y and z directions are the print (filament) and build directions, respectively

shear locking and reduce volumetric locking, reduced integration eight-node brick elements (specified with C3D8RT in ABAQUS) are used. The samples are individually meshed with ~ 4×10^6 elements. The shape of elements is cubic with the edge size of 31.25 μm. The framework below is implemented in ABAQUS 2018 in conjunction with MATLAB, Python and FORTRAN based pre and post processors.

Constitutive Relations

A finite deformation framework is used. Under the basic kinematic assumption, the deformation gradient ($\mathbf{F}$), the rate of deformation ($\mathbf{D}$), and the spin tensor ($\mathbf{\Omega}$) can be broken down to elastic and plastic parts as

$$\left.\begin{aligned}\mathbf{F} &= \mathbf{F}^e \cdot \mathbf{F}^p,\\ \mathbf{D} &= \mathbf{D}^e + \mathbf{D}^p,\\ \mathbf{\Omega} &= \mathbf{\Omega}^e + \mathbf{\Omega}^p.\end{aligned}\right\} \tag{1}$$

In the above equations, the superscripts "e" and "p" refer to the elastic and plastic parts of each tensor, respectively. The Jaumann rate of the Kirchhoff stress ($\hat{\boldsymbol{\tau}}$) is

$$\hat{\boldsymbol{\tau}} = \mathbf{L} : (\mathbf{D} - \mathbf{D}^p), \tag{2}$$

where $\mathbf{L}$ denotes the tensor of elastic moduli

$$\mathbf{L} = \frac{E}{1+\upsilon}\left[\mathbf{I}' + \frac{\upsilon}{1-2\upsilon}\mathbf{I}\otimes\mathbf{I}\right]. \tag{3}$$

Here, E is the Young's modulus, υ is the Poisson's ratio, $\mathbf{I}$ is second-order identity tensor, $\mathbf{I}'$ is fourth-order identity tensor, and "⊗" refers to the tensor product of two vectors.

The linear Drucker–Prager pressure-dependent model is used to determine the onset of plastic deformation and failure. The yield surface is defined by

$$\phi(\sigma_{ij}) = \sigma_e - \sigma_H \tan\beta - \left(1 - \frac{1}{3}\tan\beta\right)\overline{\sigma}_c = 0, \tag{4}$$

where σ_e is the von Mises equivalent stress, and $\sigma_H = (\sigma_{11} + \sigma_{22} + \sigma_{33})/3$ is the hydrostatic stress, β is the friction angle of the material in the meridional stress plane, and $\overline{\sigma}_c$ is the flow stress in compression. Here, $\tan\beta$ is referred to as the pressure sensitivity index and expressed in the form of

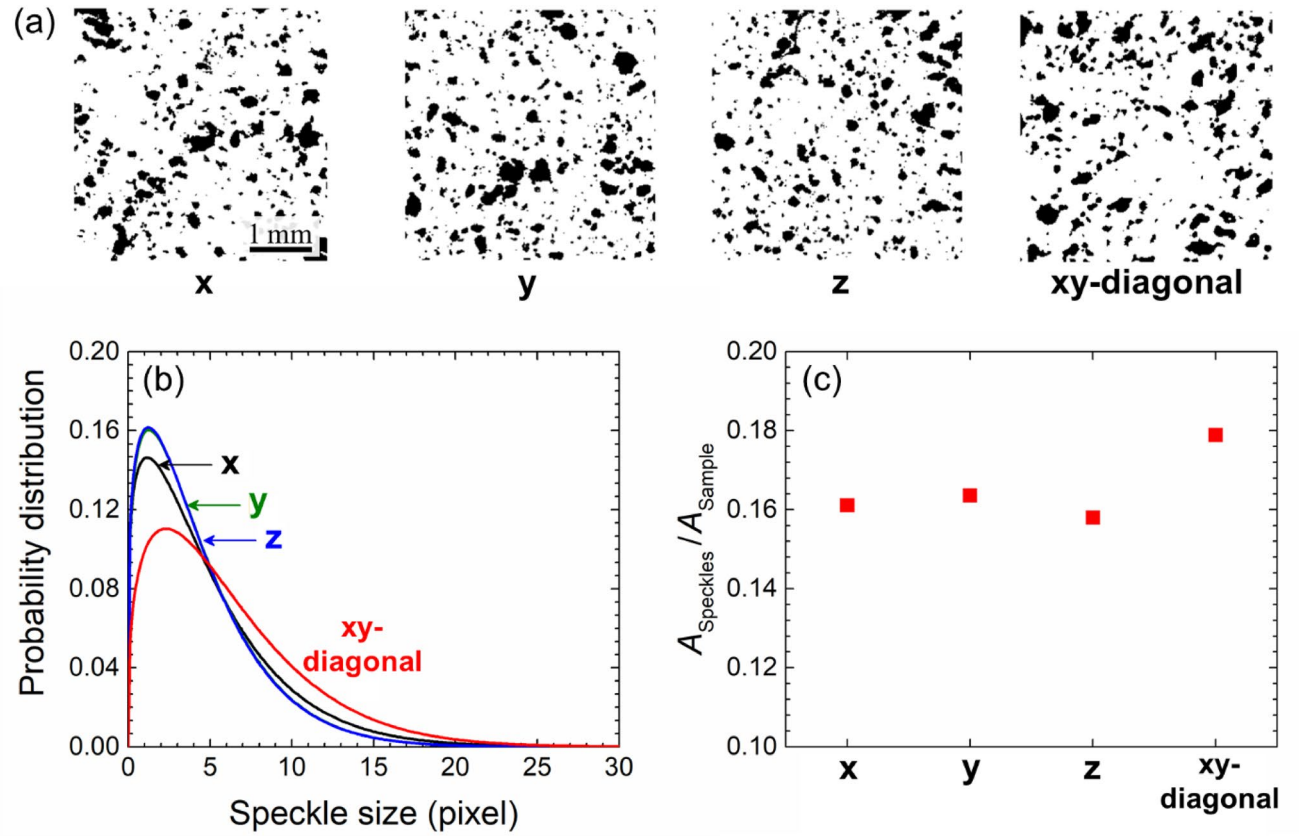

Fig. 5 **a** Speckle patterns sprayed on the samples for DIC analysis, **b** probability density distributions of the speckle dimensions, and **c** area fractions of the samples covered by the speckles

$$\tan\beta = 3\frac{m-1}{m+1}, \tag{5}$$

where $m = \sigma_c/\sigma_t$ is the ratio of the yield point in compression to that in tension (σ_t), and for polymers $m \simeq 1.3$ [37]. The strain rate effect on the flow stress is accounted by the Johnson–Cook strain rate dependence law as

$$\overline{\sigma}_c = \sigma_c(1 + C\ln\dot{\varepsilon}^*), \tag{6}$$

where $\dot{\varepsilon}^* = \dot{\overline{\varepsilon}}^{pl}/\dot{\varepsilon}_0$ in which $\dot{\overline{\varepsilon}}^{pl}$ and $\dot{\varepsilon}_0$ are the equivalent plastic strain rate and the reference strain rate, respectively. σ_c is the yield strength corresponding to $\dot{\varepsilon}^* = 1$. C is a material constant and selected to be 0.005 based on a qualitative comparison of the results from the computations and the experiments.

The volumetric behavior is described by the linear $U_s - U_p$ Hugoniot form of the Mie-Grüneisen equation of state (EOS),

$$p = -\sigma_H = \frac{\rho_0 c_0^2 \eta}{(1-s\eta)^2}\left(1 - \frac{\Gamma_0\eta}{2}\right) + \Gamma_0\rho_0 E_m. \tag{7}$$

Here, ρ_0 is density in the reference configuration, $\eta = 1 - \rho_0/\rho$ is the nominal volumetric compressive strain, Γ_0 is Grüneisen's gamma at the reference state and for polymers $\Gamma_0 \simeq 1$, E_m is the internal energy per unit mass, and c_0 and s define the linear relationship between the shock velocity U_s and the particle velocity U_p via

$$U_s = c_0 + sU_p. \tag{8}$$

For the AMEM simulant analyzed, $c_0 = 2315.4$ m/s and $s = 1.905$. The effect of load orientation on c_0 and s is negligible [36].

To resolve arbitrary failure patterns which are unknown a priori, a failure criterion based on maximum equivalent plastic strain is used for all elements. The failure criterion is met when the equivalent plastic strain $\overline{\varepsilon}^{pl}$ in an element reaches the critical level of $\overline{\varepsilon}_f^{pl}$. Once this condition is met in an element, the element is considered to have failed and have no further strength. The values of $\overline{\varepsilon}_f^{pl}$ for all material sets are listed in Table 2. A proper contact state in active contact surfaces is achieved with a penalty force algorithm. Friction between surfaces in contact is evaluated

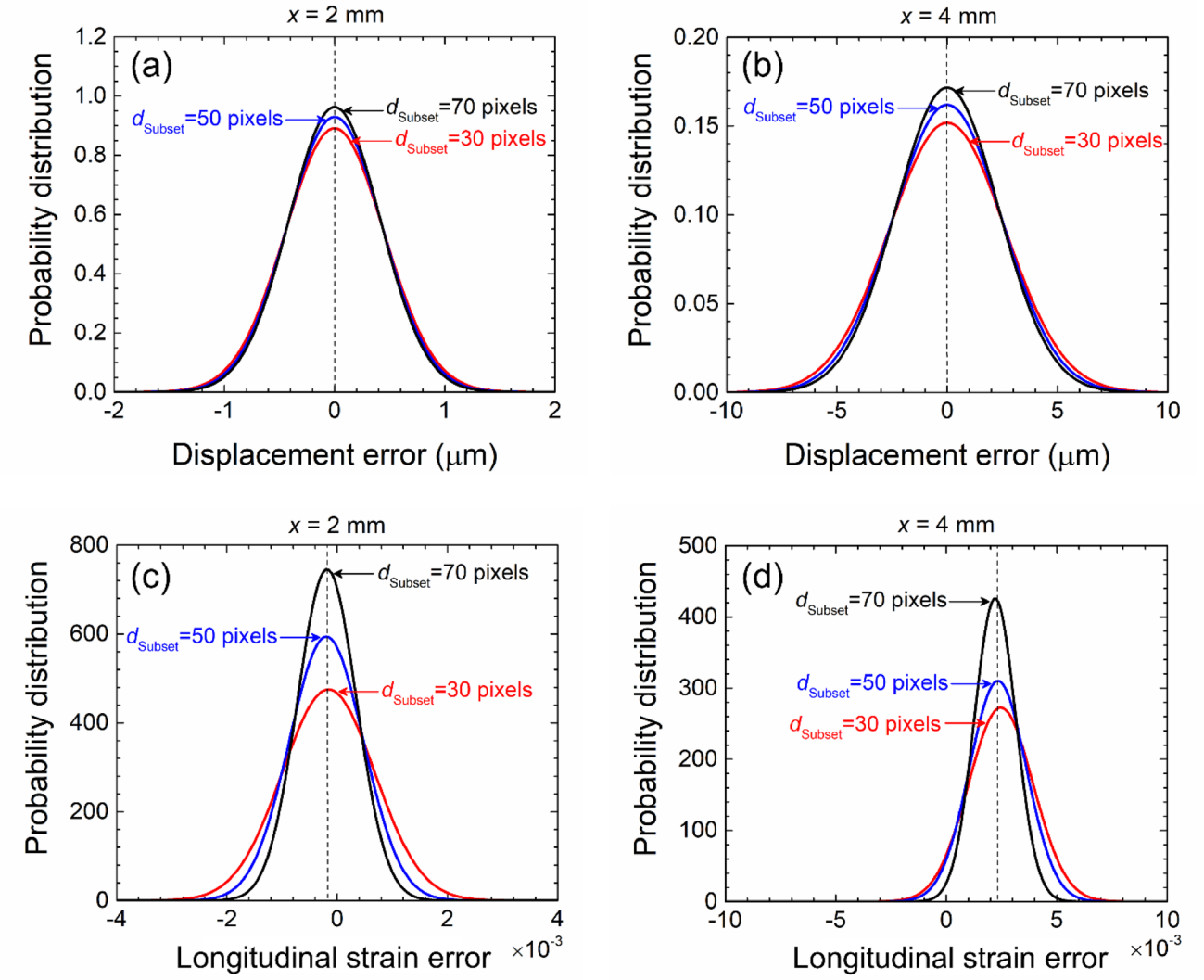

Fig. 6 Probability density distributions of the errors in the displacement and longitudinal strain obtained by rigidly translating a sample by $x = 2$ and 4 mm

according to the Coulomb friction law. Consequently, the frictional heating rate is

$$\dot{W}^{fric} = \frac{1}{\Delta V} \int_{\Delta S} \mu \sigma_n v_{rel} dS, \tag{9}$$

where ΔV is the material volume subjected to heating, μ is the coefficient of friction which is taken as 0.5 for all surfaces in contact, ΔS is the contact surface area, σ_n is the normal contact stress, and v_{rel} is the relative sliding velocity between the surface pair in contact. The value of the coefficient of friction is selected according to data available in the literature for polymer-bonded explosives [38]. Heat conduction follows Fourier's law. The specific heat for the material is estimated to be 1500 J kg^{-1} K^{-1}.

Results

Experiments and Model Validation

The results obtained through computations are quantitatively and qualitatively compared with those obtained from experiments. The experiments are performed at an average loading rate of ~ 310 s^{-1}. The computations are carried out at a constant strain rate of ~ 310 s^{-1}, and with this approximation, the maximum difference between the overall strain in experiments and computations at is 0.02. The deformation modes, the time and strain at damage initiation, and temperature signatures are compared. The samples are deformed beyond the pulse duration 200 μs due to secondary waves. Deformation of samples continues up to $t = 600$ μs and an overall strain of ~ 20%. Figure 8a

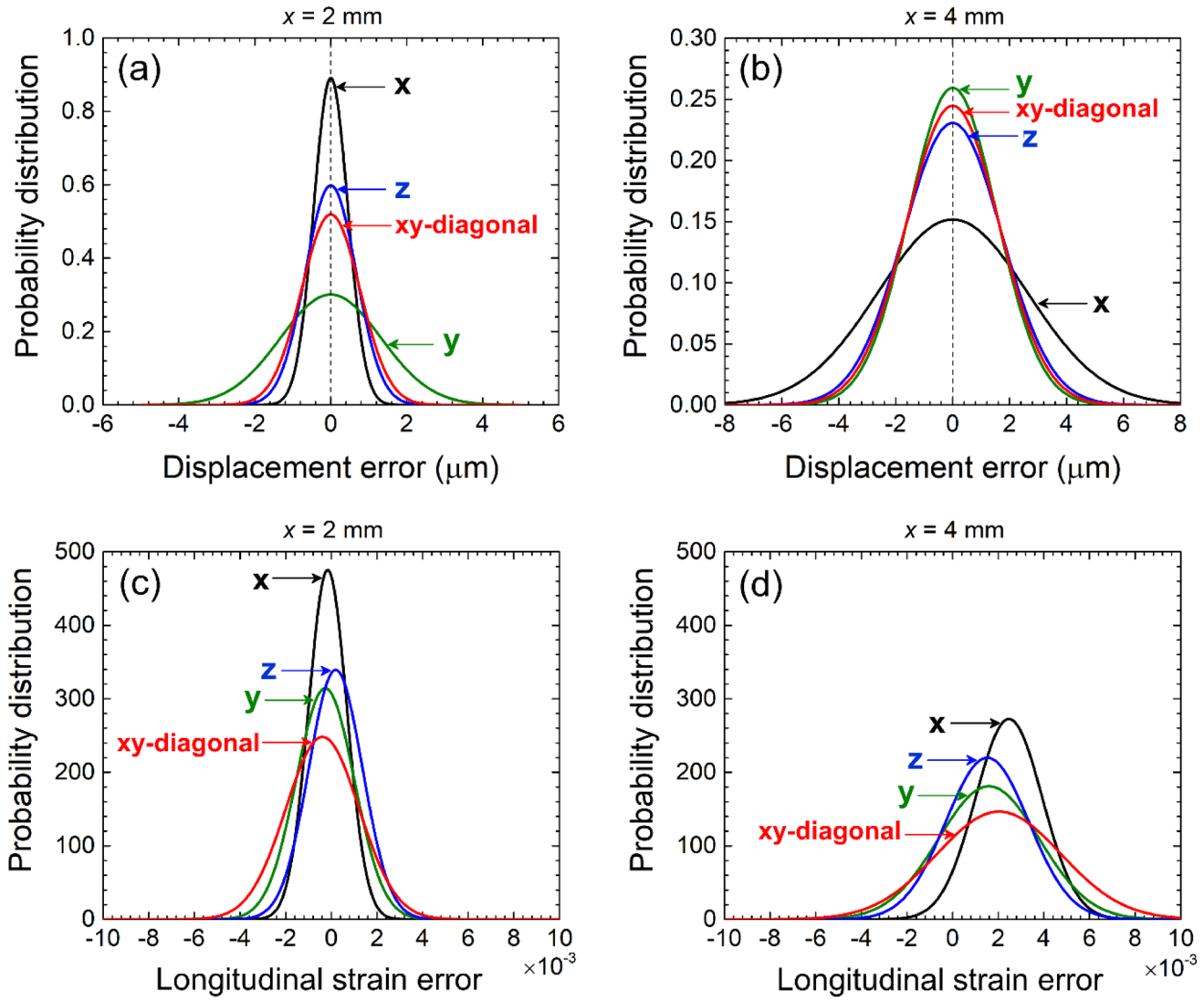

Fig. 7 Probability density distributions of the errors in the displacement and longitudinal strain calculations for different loading directions obtained by rigidly translating the samples by $x = 2$ and 4 mm. The subset size is 30 pixels

Table 2 Material property sets used in the simulations

Material sets	Density (gr/cm^3)	E(GPa)	σ_c(MPa)	ε_c(%)	$\bar{\varepsilon}_f^{pl}$(%)
Filaments-set 1 (blue filaments)	1.6	0.5	15.0	3.0	60
Filaments-set 2 (green filaments)	1.6	2.5	22.5	0.9	60
Filaments-set 3 (red filaments)	1.6	4.5	30.0	0.7	60
Inter-filament surfaces	1.1	2.5	22.5	0.9	40
Inter-filament voids	0.5	0.5	15.0	3.0	20

$\bar{\varepsilon}_f^{pl}$ is the equivalent plastic strain at failure

shows the time histories of the overall engineering strain $\bar{\varepsilon} = (L - L_0)/L_0$ from the experiments and computations. L is the instantaneous length of a sample and $L_0 = 5$ mm is the initial length. This strain is measured by tracking the positions of the indenters through the VL images. Both computations and experiments show fracture at or after ~ 200 μs of loading, with the onset of failure at overall strains in the range of 3.4–5.9%. The onset of fracture is indicted by "•", with solid lines before this symbol denoting unfractured states and dash lines after this symbol

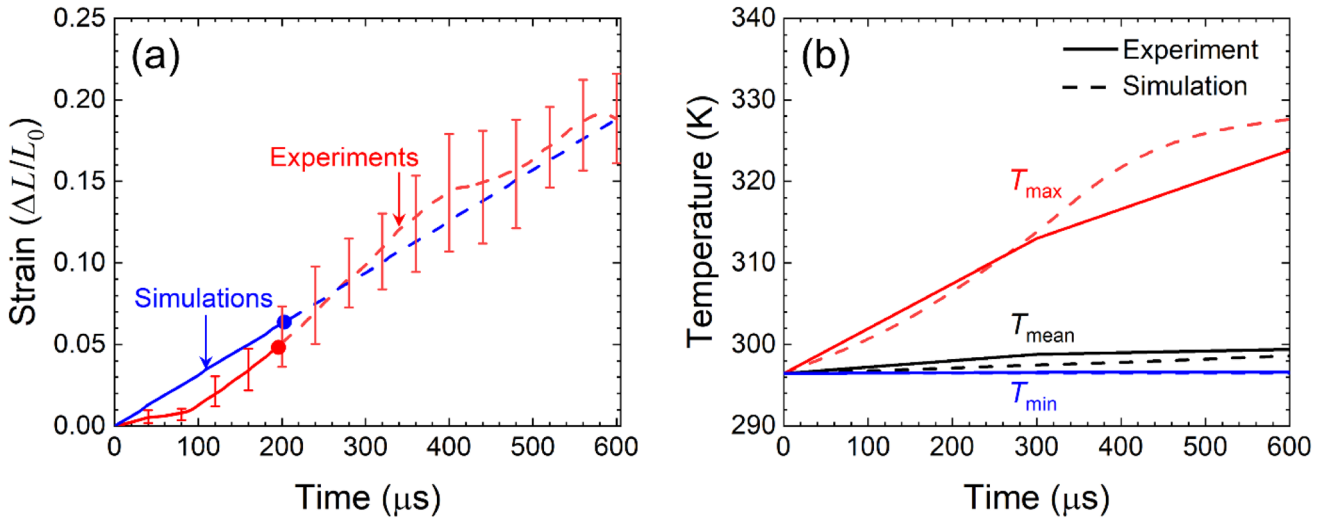

Fig. 8 Comparison of measured and calculated overall strain levels as a function of time. The onset of rupture is indicted by "•", with solid lines before this symbol denoting un-ruptured states and dash lines after this symbol denoting post-rupture deformation. The error bars show the variation of the overall strain levels among the multiple samples. **b** Comparison of measured and calculated lowest, mean, and highest temperature levels

denoting post-fracture deformation. The infrared images are captured at $t = 300$ and 600 μs.

Figure 8b compares the lowest, average, and highest temperature levels obtained from the simulations and the experiments. The superscripts "Exp." and "Sim." denote experimental measurements and simulations, respectively. The calculated temperatures are in very good agreement with the experimentally measured temperatures, with the error being only ~ 3.9 K in the highest temperatures at $\bar{\varepsilon} = 0.19$ and $t = 600$ μs. At this time, the maximum error in the temperature increase between the computations and the experiments is ~ 14.0%. The agreement provides one validation of the computational model.

Damage Initiation and Crack Nucleation Sites

Figure 9 shows a sequence of VL images for the sample loaded in the x (⊥ print) direction (see Fig. 4). Under loading, the sample shows shear deformation and shear rupture. To quantify the deformation fields in the samples, digital image correlation (DIC) analyses are performed. A total of 4 samples are studied at similar conditions. The DIC analyses concern the deformation fields up to the onset of shear rupture which occurs around $t = 170 - 220$ μs or overall strains of 3.4–5.9% for the sample set. Figure 10 shows the distributions of the maximum in-plane tensorial shear strain $(\gamma_{max}/2)$ in the samples at the onset of rupture as calculated via

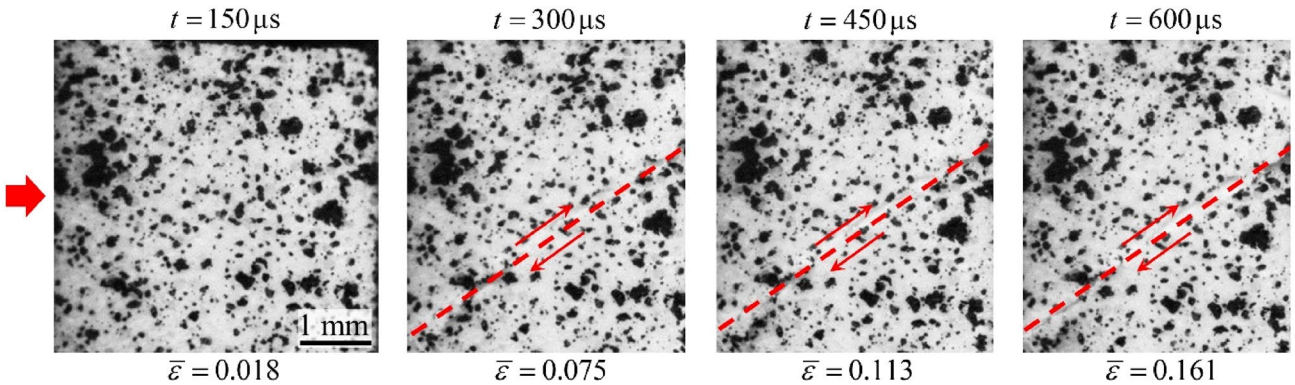

Fig. 9 Deformation for loading in the x-direction. The dashed lines and the arrows outline the rupture process and the relative motion

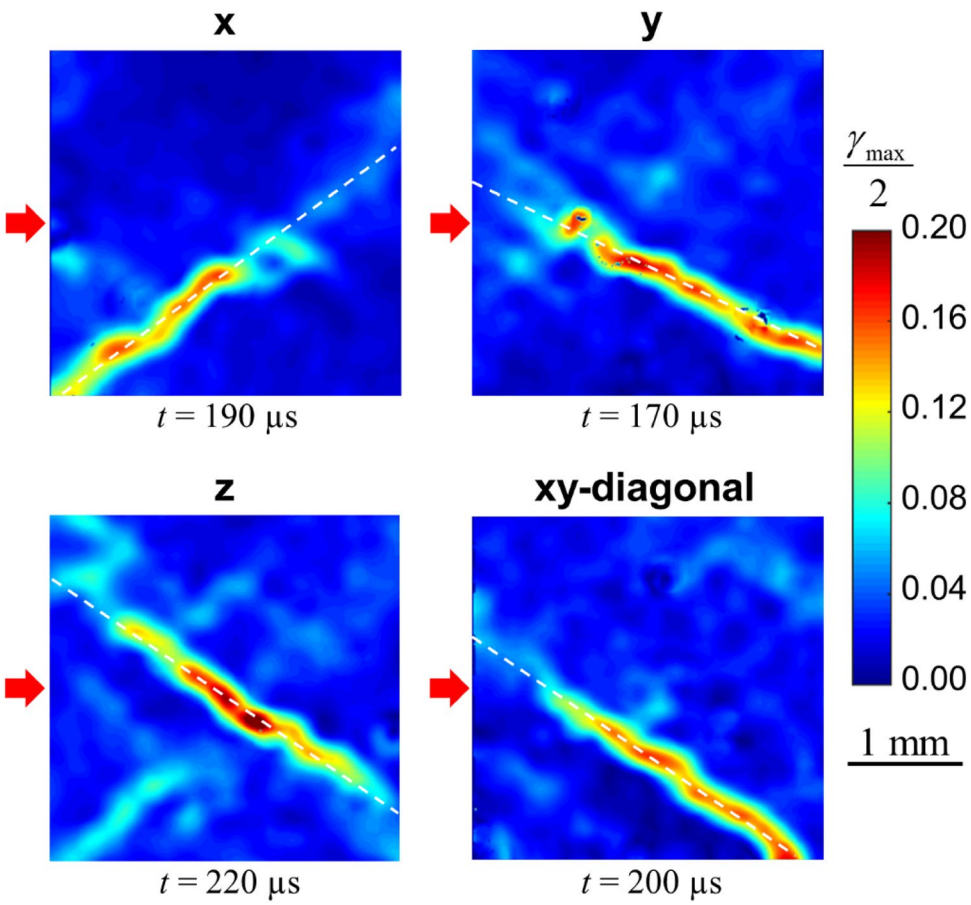

Fig. 10 Distributions of the maximum tensorial shear strain $(\gamma_{max}/2)$ calculated at the rupture nucleation

$$\frac{\gamma_{max}}{2} = \sqrt{\left(\frac{E_{xx} + E_{yy}}{2}\right)^2 + E_{xy}^2}, \tag{10}$$

where E_{xx}, E_{yy}, and E_{xy} are the Lagrangian strain components. The local maximum shear strain level at rupture is $4.8 \pm 0.8\%$. The DIC calculation is carried out using a subset size of 30 pixels (408 μm). Note that post rupture, this shear strain continues to increase and can reach values up to 20%. The shear band angle with respect to the loading direction is $33.6 \pm 5.3°$. A similar value for the shear band angle was previously observed in a polymer bounded composite tested in an SHPB environment [23]. The material properties obtained and the physics captured in the experiments are used to inform the simulations. Table 3 quantifies the average and maximum strain rate, overall compression strain at onset of fracture, fracture initiation time, the overall strain at fracture initiation, and overall total compression for all samples analyzed.

In the experiments, shear bands nucleate from the edge of the samples for loading in the x, y, or xy-diagonal directions. For loading in the z-direction, the dominant shear band nucleates from an internal point rather than the edge, due to internal heterogeneities. It is difficult to experimentally relate the crack nucleation sites to the print structure due to the opaque nature of the sample. The computations, on the other hand, offer an opportunity to track the crack paths in the sample's interior. Here, it is assumed that samples

Table 3 Summary of experiments

No	Loading direction	Maximum strain rate (s^{-1})	Average strain rate (s^{-1})	Fracture time (μs)	Overall strain at fracture	Overall compression
1	x	675	268	190	0.034	0.161
2	y	950	343	170	0.053	0.206
3	z	425	283	220	0.059	0.170
4	xy-diagonal	1100	360	200	0.044	0.216

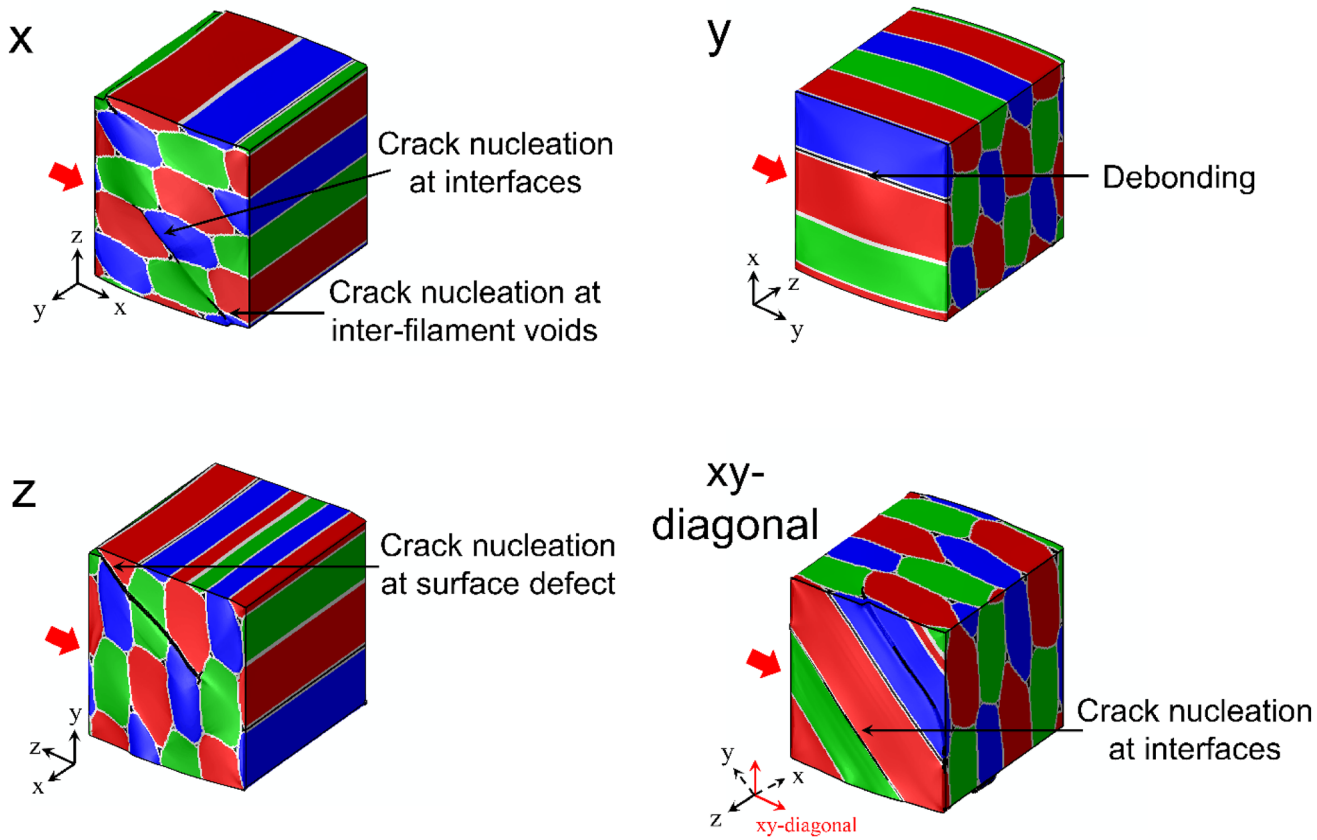

Fig. 11 Fracture initiation for different loading directions at $\bar{\varepsilon} = 0.064$ or $t = 204\,\mu s$

are initially crack-free and cracks result from the loading events. The computations account for failure at all possible sites, inside the filaments and along the interfaces. Figure 11 shows the fracture initiation sites in samples loaded along the four direction at $\bar{\varepsilon} = 0.064$ or $t = 204\,\mu s$. Cracks nucleate at or before $\bar{\varepsilon} = 0.064$ or $t = 204\,\mu s$. The nucleation is at the filament junctions and propagates through the filaments. The sample loaded in the y-direction (along the filaments)

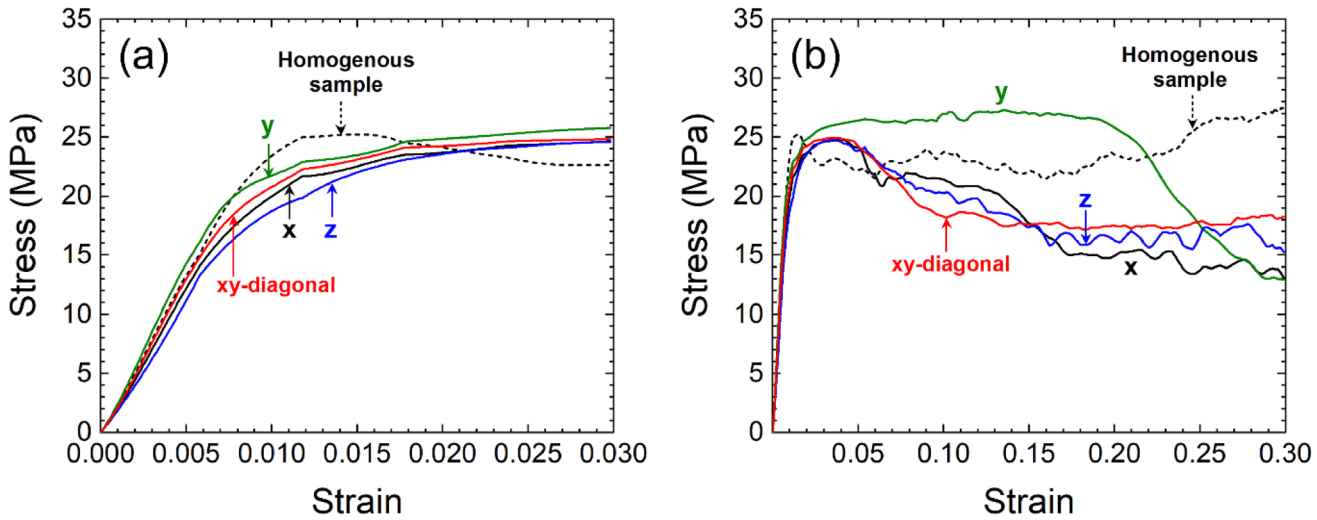

Fig. 12 Stress-strain curves for loading in the x, y, z, and xy-diagonal directions: **a** strain levels up to 0.03 and **b** strain levels up to 0.3

does not experience significant fracture at this stage, and instead shows only minor crack development and interfacial debonding along the loading direction at the later stage of $\overline{\varepsilon} = 0.31$ when the other loading directions show extensive crack development throughout the sample. The effects of the orientation-dependent fracture strain levels on the overall stress-strain relations are discussed in the next section.

Stress–Strain Curves

Figures 12a and b show the overall stress-strain relations for the four loading orientations. For comparison, a calculation is also carried out for the homogeneous sample (without microstructure or heterogeneities) having the properties of the base material as measured from the quasi-static uniaxial compression experiments (see Table 1). Specifically, Fig. 12a shows the overall stress-strain relations for the early stages of loading up to $\overline{\varepsilon} = 0.03$. The sample loaded along the filaments (y-direction) shows a higher level of initial stiffness than the samples loaded perpendicular to the filaments (x or z direction). This is in agreement with the trend seen in experiments (see Table 1). The homogenized sample achieves the highest level of stress among all samples at the end of elastic region $\left(\overline{\varepsilon} = 0.012,\ \overline{\sigma} = 25.7\ \text{MPa}\right)$. Beyond this point, the homogenized sample shows more pronounced damage initiation such that the overall stress level becomes the lowest among all samples at $\overline{\varepsilon} = 0.03$.

Figure 12b shows the stress-strain relations for overall strain levels up to 0.3. Overall in later stages, the sample loaded in the y-direction sustains a higher level of stress relative to the samples loaded in the other orientations. This sample even has a stress level that is higher than the stress level of the homogeneous sample up to $\overline{\varepsilon} = 0.2$. This is due to the fact that the material undergoes minor damage and consequently experiences lower loss of stiffness. When the sample is loaded in the y-direction (along filaments), the initiation of damage is in the form of debonding sites parallel to the loading directions. The overall stress state in the sample does not result in major tension or shear at the tips of the cracks parallel to the loading direction. Therefore, the evolution of damage is relatively slow. In the homogenized sample, the cracks nucleate approximately at the 45-degree angles relative to the loading direction where maximum shear occurs, consequently, damage propagates at a higher rate than the sample loaded in the y-direction. In contrast, the homogeneous sample sustains higher stress levels than the samples loaded in x, y and xy-diagonal directions. For these loading directions, portions of the microstructure interfaces are oriented at or close to the maximum shear planes. Since the damage initiation threshold levels at the interfaces are lower than the levels in the base material or the filaments, damage initiation is facilitated by the material microstructure. In summary, depending on the loading orientation,

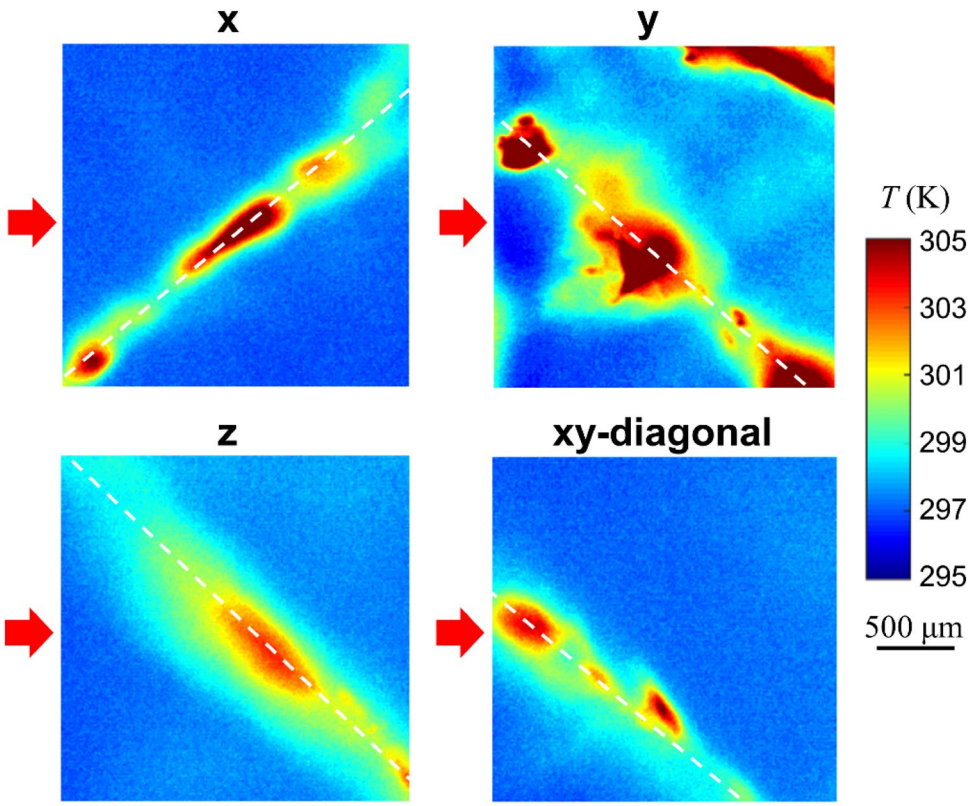

Fig. 13 Experimentally measured temperature fields in the samples loaded in the x, y, z, and xy-diagonal directions at $\overline{\varepsilon} = 0.19$ or $t = 600$ μs

the microstructure morphology can significantly affect the material integrity and stress-carrying capability.

Temperature Distributions

Plastic deformation and internal friction result in heating in the samples. Experimentally, it is challenging to separate the contributions of these mechanisms, but their combined effects are captured. Figure 13 shows the experimentally measured temperature fields in the four samples at $\overline{\varepsilon} = 0.19$ or $t = 600$ µs. The loading conditions are listed in Table 3. The IR integration time is 50 µs. This value is selected according to calibration data to achieve an accuracy of 0.5 K for temperature measurements between 300–350 K. Significant temperature increases occur along the shear bands, with the highest temperatures occurring at the centers of the bands. There is no appreciable temperature increase far away from the shear bands. The maximum temperature increases in the samples is 27.4 ± 0.5 K, with a 0.5 K measurement error according to calibration data. Intense shear and the temperature increases occur primarily in shear bands in a localized fashion. The development of such hotspots is of primary interest for energetic materials, as they may lead to the initiation of chemical reaction. To quantify the spatial distribution and the extent of localization of heating, the temperature fields in Fig. 14 are further analyzed by calculating the fractions of the sample area with each temperature. This allows the degree of heating localization to be compared across different cases. Figure 14a shows the results of the analysis. The vertical axis can be interpreted as the probability of a random point on the sample surface to assume a certain temperature at $t = 300$ and 600 µs (corresponding strains are ~ 0.10 and ~ 0.19). This axis can also be interpreted to be the proportions of the sample surface having any given temperature in the range shown. The dominant temperatures in the samples (the temperature that is associated with the highest proportion of the material surface) are ~ 296–299 K. The highest temperatures in the samples are ~ 324 K and occurs mostly in the smaller regions where the samples undergo intense shear inside and around the shear bands.

The orientation dependence of the temperature distributions can be observed through computations. Figure 14b shows how localized or spread out spatially the heating is. Loading in the xy-diagonal direction yields the highest temperatures. In contrast, loading in the other directions lead to less concentrated heating and higher fractions of the material participate in the deformation and heating at the lower end of the temperature range. The homogeneous sample has the least concentration of heating, as expected.

Displacement, Velocity and Temperature Profiles Along Shear Bands

Post rupture, the deformation fields on the two sides of the shear band are calculated separately using different regions of interest (ROIs). The edges of the ROIs next to the shear bands are ~ 0.2 mm (15 pixels, the subset radius) from the shear band center line. For loading in the x-direction, Fig. 15 shows the horizontal and vertical displacement fields and the corresponding temperature fields at $t = 300$ and 600 µs. Rupture occurs at $t = 200$ µs. The displacement field on each side of the shear band is approximately uniform. There is no appreciable temperature increase away from the shear band. Significant temperature increases occur along the shear bands, with the highest temperatures occurring at the

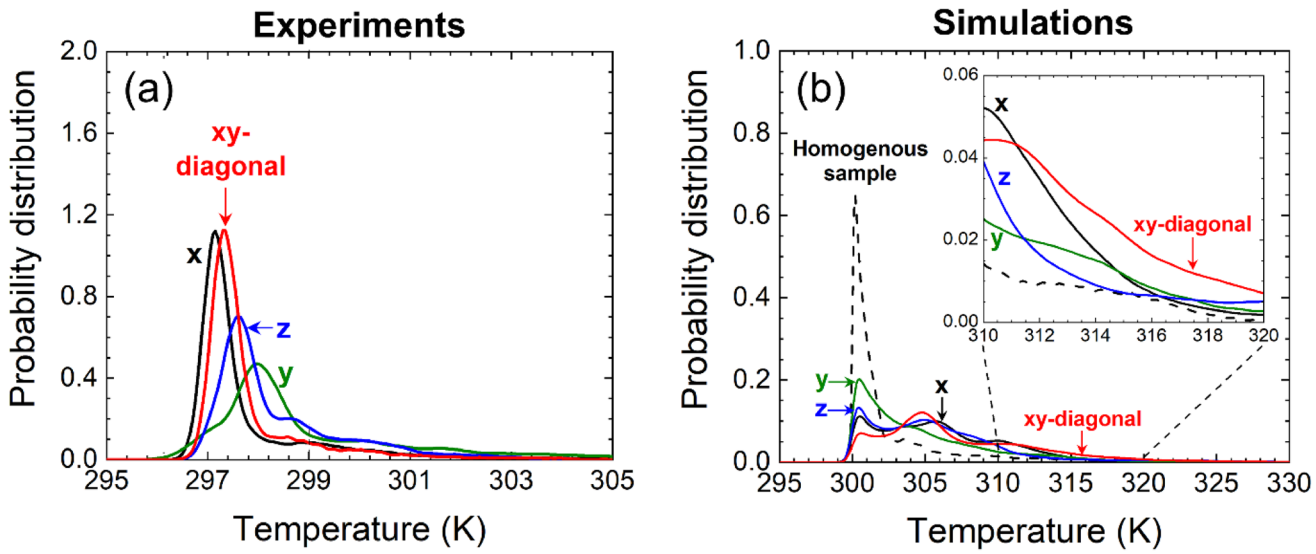

Fig. 14 Temperature distributions for different loading directions at $t = 600$ µs: **a** experiments, and **b** computations

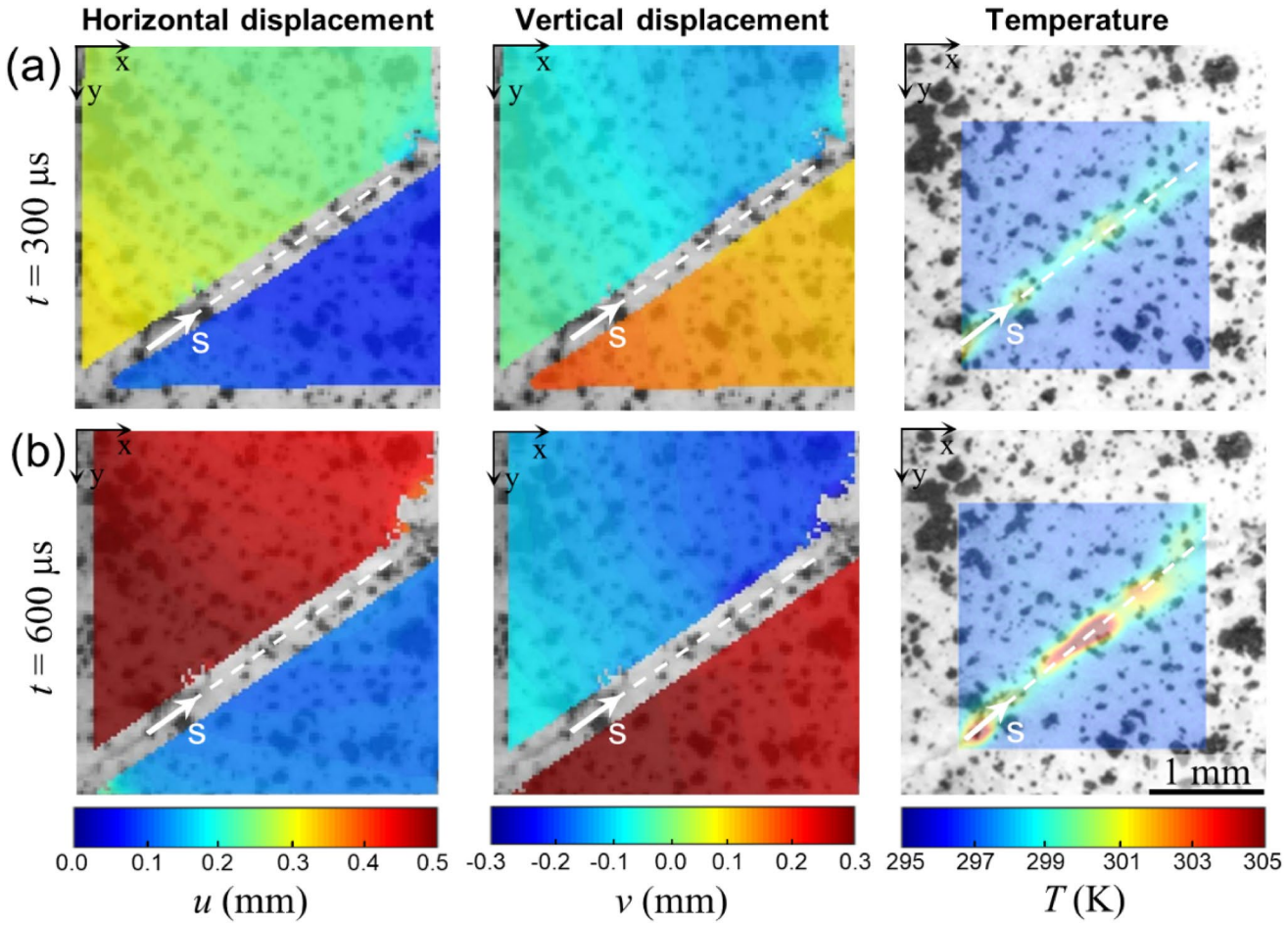

Fig. 15 Displacement and temperature fields in the sample loaded in the x-direction at **a** $t = 300$ µs and **b** $t = 600$ µs

centers of the bands. The s-axis in the figure indicates the distance along the shear bands referred to in the rest of this paper.

Figure 16 compares the profiles of the relative displacement and velocity across the shear bands (displacement and velocity jumps) with the temperature profiles at $\bar{\varepsilon} = 0.19$ or $t = 600$ µs. The horizontal axis presents the distance along the bands. For loading in the x-direction, the shear band-parallel displacement and transverse velocity jump are relatively uniform along the bands, indicating relatively homogeneous slip along the shear band path (s-axis). However, the corresponding temperature profiles along the shear band are quite non-uniform. The displacement and velocity jump for the y, z, and xy-diagonal directions show significant variations along the bands. In general, there is a correlation between the magnitudes of the relative displacement and velocity jump, their non-uniformity along the bands, and the temperature increases. The non-uniformity appears to be associated with the heterogeneous nucleation of cracks along the shear band paths. Higher and faster relative slip tend to give rise to higher local temperature increases. For example, for loading in the y-direction, the location of the peak temperature at $t = 600$ µs (~ 324 K) coincides with the location of displacement and velocity jump change along the shear band path.

Energy Dissipation levels

Dissipations from friction and plastic deformation turn into heat and contribute to the temperature increase in the samples. The dissipation mechanisms (friction and plasticity) and their relative contributions to heating are analyzed as functions of the loading orientations. Computations are performed for a time period of 1000 µs, which is longer than the 600 µs period of experiments. Figure 17a and b show the contributions to dissipation by plastic deformation $\left(W_P\right)$ and fiction $\left(W_F\right)$, respectively. Overall, the contribution of internal friction is orders of magnitude lower than that of plasticity. Loading in the y-direction results in the highest plastic dissipation but lowest frictional dissipation. In contrast, loading in the xy-diagonal direction leads to lowest plastic dissipation but highest frictional dissipation. This

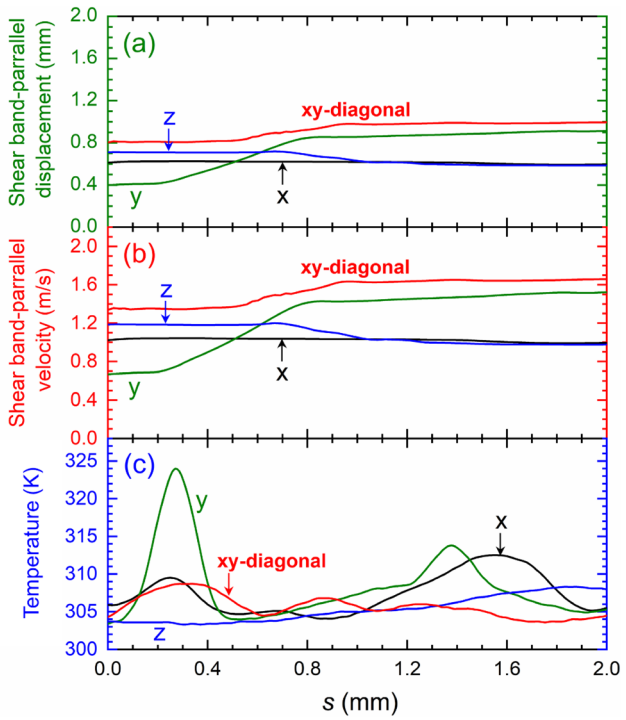

Fig. 16 **a** Profiles of relative displacement, **b** velocity jump across shear bands, and **c** temperature along the shear bands at $t = 600$ μs

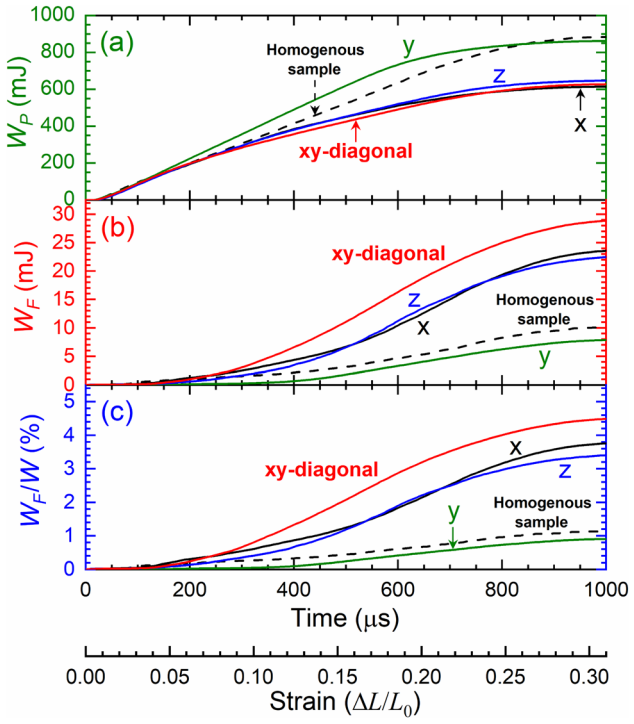

Fig. 17 **a** Plastic dissipation levels, **b** frictional dissipation levels, and **c** friction dissipation as a fraction of overall dissipation as functions of time for loading in different directions

interplay is directly related to the formation of shear bands and the extent of localization of the shear deformation. In general, less damage corresponds to higher levels of stress carried by the materials which in turn lead to higher levels of inelastic/plastic dissipation. Figure 17c shows the frictional dissipation as a fraction of the overall dissipation in the samples $\left(W_F/W\right)$. Depending on the orientation, frictional dissipation is only responsible for 0.9–4.5% of the total heating and bulk plasticity accounts for the rest. Although in absolute terms, frictional dissipation is low, it plays an important role in hotspot development, owing to the fact that frictional heating is highly localized in the shear bands. The importance of frictional dissipation can be revealed by comparing the trends in frictional dissipation and the highest temperatures in the samples. The sample loaded in the xy-diagonal direction experiences the lowest overall heating, but has the highest level of frictional dissipation and the highest fraction of material volume in the peak temperature range of 310–320 K [see Fig. 14b] among all orientations. Loading in the y-direction leads to the highest level of inelastic dissipation and overall dissipation. Note that while loading in the y-direction leads to overall heating that is approximately 37.2% higher than that for loading in the xy-diagonal direction, it leads to a lower fraction of material volume having the higher temperatures in the range of 310–320 K. This is because the deformation is less localized under y-direction loading and more spread out in the material.

Summary

Experiments and simulations are performed to analyze the dynamic thermo-mechanical behavior of an AMEM simulant whose base material consists of a photopolymer and solid particles. The mesoscale deformation, failure, and heating of the material under loading along four different directions with respect to the print structure are studied. The study focuses on response anisotropy arising from the AM structures of the material. A split-Hopkinson pressure bar (SHPB) is used to apply compressive loading at an overall strain rate of 310 s^{-1}. Integrated high-speed visible light (VL) and infrared (IR) imaging is used to simultaneously measure the deformation and temperature fields over the same area of a sample with microsecond-level time resolutions and micron-level spatial resolutions. The overall field of views (FOVs) for the VL and IR images are 7.0×4.4 mm and 2.2×2.2 mm, respectively. Shear band development is the primary mechanism for deformation, heating, and ultimate failure. The influence of loading direction relative to the AM structure of the material primarily manifests through how shear bands form. Post-rupture sliding along the shear bands is the primary heating mechanism and leads to significant temperature

increases, with the highest temperature increase observed being 27.4 K. The maximum shear strains at rupture is observed to be $4.8 \pm 0.8\%$. The shear bands are observed to be $33.6 \pm 5.3°$ relative to the loading direction. The deformation and temperature profiles along the shear bands are obtained. The correlations in the variations in the profiles appear to coincide with the nucleation of rupture out of material heterogeneities and defects.

An experimentally-informed Lagrangian finite element framework is developed that accounts for finite-strain elastic–plastic deformation, strain-rate effect, arbitrary failure initiation and propagation, post contact and friction, heat generation resulting from friction and inelastic bulk deformation, and heat conduction. The microstructures used in the simulations are generated based scanned morphologies of the real material. Simulations performed focus on failure initiation and the contributions to heating, and interplays between plasticity and internal friction. The results show that cracks nucleate at the filament junctions and propagate through filaments. Loading in the print direction leads to minor damage and higher stresses compared with other loading directions. Loading at 45-degree with respect to the print orientation (xy-diagonal direction) leads to lower stresses, more intense shear banding and higher temperatures. The simulations further reveal that intense shear leads to more significant contributions of internal friction to heating and higher fractions of the material volume that attain higher temperatures. Overall, frictional dissipation accounts for only 0.9–4.5% of heating with plasticity responsible for the rest. Despite of this disparity, friction plays an important role in hotspot development, owing to the fact that it is much more localized and occurs primarily in the interior of intensely formed shear bands.

The analyses so far have focused on uni-directionally printed materials with low overall porosities. Further studies should also consider other structures and wider ranges of heterogeneities.

Acknowledgements The authors gratefully acknowledge support from DTRA through Project No. HDTRA1-18-1-0004 (Dr. Jeffery Davis). We would like to thank Didier Montaigne at the Air Force Research Lab at Eglin AFB for providing the materials used in the study. The experiments were performed at the Dynamic Property Research Laboratory (DPRL) at Georgia Tech.

Authors Contributions Conceptualization: AK, MZ; Methodology: AK, MZ; Formal analysis and investigation: AK; Writing—original draft preparation: AK; Writing—review and editing: MZ; Funding acquisition: MZ; Resources: MZ; Supervision: MZ.

Funding This research was funded by DTRA (Project No. HDTRA1-18-1-0004).

Data Availability Datasets supporting the conclusion of this article are available on demand.

Compliance with Ethical Standards

Conflict of interests The authors declare that they have no conflicting of interests.

References

1. Herzog D, Seyda V, Wycisk E, Emmelmann C (2016) Additive manufacturing of metals. Acta Mater 117:371–392. https://doi.org/10.1016/j.actamat.2016.07.019
2. Frazier WE (2014) Metal additive manufacturing: a review. J Mater Eng Perform 23(6):1917–1928. https://doi.org/10.1007/s11665-014-0958-z
3. Wong KV, Hernandez A (2012) A review of additive manufacturing. ISRN Mech Eng 1:1–10. https://doi.org/10.5402/2012/208760
4. Murray AK, Isik T, Ortalan V, Gunduz IE, Son SF, Chiu GT-C, Rhoads JF (2017) Two-component additive manufacturing of nanothermite structures via reactive inkjet printing. J Appl Phys 122(18):184901. https://doi.org/10.1063/1.4999800
5. Clark B, Zhang Z, Christopher G, Pantoya ML (2017) 3D processing and characterization of acrylonitrile butadiene styrene (ABS) energetic thin films. J Mater Sci 52(2):993–1004. https://doi.org/10.1007/s10853-016-0395-5
6. Wang H, DeLisio JB, Jian G, Zhou W, Zachariah MR (2015) Electrospray formation and combustion characteristics of iodine-containing Al/CuO nanothermite microparticles. Combust Flame 162(7):2823–2829. https://doi.org/10.1016/j.combustflame.2015.04.005
7. Wang H, Jian G, Egan GC, Zachariah MR (2014) Assembly and reactive properties of Al/CuO based nanothermite microparticles. Combust Flame 161(8):2203–2208. https://doi.org/10.1016/j.combustflame.2014.02.003
8. Huang C, Jian G, DeLisio JB, Wang H, Zachariah MR (2015) Electrospray deposition of energetic polymer nanocomposites with high mass particle loadings: a prelude to 3D printing of rocket motors. Adv Eng Mater 17(1):95–101. https://doi.org/10.1002/adem.201400151
9. Ihnen AC, Lee WY, Fuchs B, Petrock AM, Stec III D (2016) Ink jet printing and patterning of explosive materials. U.S. patent 9,296,241 B1.
10. Ruz-Nuglo F, Groven L, Puszynski JA (2014) Additive manufacturing for energetic components and materials. 50th AIAA/ASME/SAE/ASEE Joint Propulsion Conference, p 3894. https://doi.org/10.2514/6.2014-3894
11. Tappan AS, Ball JP, Colovos JW (2012) Inkjet Printing of Energetic Materials: Sub-Micron Al/MoO3 and Al/Bi2O3 Thermite. Sandia National Laboratories Presentation SAND2011-8957C, Albuquerque, NM (United States).
12. Fleck TJ, Murray AK, Gunduz IE, Son SF, Chiu GTC, Rhoads JF (2017) Additive manufacturing of multifunctional reactive materials. Addit Manuf 17:176–182. https://doi.org/10.1016/j.addma.2017.08.008
13. Stansbury JW, Idacavage MJ (2016) 3D printing with polymers: challenges among expanding options and opportunities. Dent Mater 32(1):54–64. https://doi.org/10.1016/j.dental.2015.09.018
14. Oropallo W, Piegl LA (2016) Ten challenges in 3D printing. Eng Comput 32(1):135–148. https://doi.org/10.1007/s00366-015-0407-0
15. Lee C, Kim S, Kim H, Ahn S (2007) Measurement of anisotropic compressive strength of rapid prototyping parts. J Mater Process Technol 187:627–630. https://doi.org/10.1016/j.jmatprotec.2006.11.095

16. Ahn S-H, Montero M, Odell D, Roundy S, Wright PK (2002) Anisotropic material properties of fused deposition modeling ABS. Rapid Prototyp J 8(4):248–257. https://doi.org/10.1108/13552540210441166
17. Mueller A, Schmalzer A, Bowden P, Tappan B, White A, Menikoff R (2019) Diameter effects on the directional anisotropic detonation behavior of strand structured additively manufactured explosives. 21st Biennial Conference of the APS Topical Group on Shock Compression of Condensed Matter, Portland, OR, June 16-21, Vol. 64.
18. O'Grady C, Tappan A, Knepper R, Rupper S, Vasiliauskas J, Marquez M (2019) Investigating typical additive manufacturing defect geometries using physical vapor deposition explosives as a model system. 21st Biennial Conference of the APS Topical Group on Shock Compression of Condensed Matter, Portland, OR, June 16-21, Vol. 64.
19. Keyhani A, Kim S, Horie Y, Zhou M (2019) Energy dissipation in polymer-bonded explosives with various levels of constituent plasticity and internal friction. Comput Mater Sci 159:136–149. https://doi.org/10.1016/j.commatsci.2018.12.008
20. Field J, Bourne N, Palmer S, Walley S, Sharma J, Beard B (1992) Hot-spot ignition mechanisms for explosives and propellants [and discussion]. Philos Trans R Soc Lond A 339(1654):269–283. https://doi.org/10.1098/rsta.1992.0034
21. Field JE, Swallowe GM, Heavens SN (1982) Ignition mechanisms of explosives during mechanical deformation. Proc R Soc Lond A Math Phys Sci 382(1782):231–244. https://doi.org/10.1098/rspa.1982.0099
22. Skidmore C, Phillips D, Asay B, Idar D, Howe P, Bolme D (2000) Microstructural effects in PBX 9501 damaged by shear impact. AIP Conf Proc 505:659–662. https://doi.org/10.1063/1.1303559
23. Ravindran S, Tessema A, Kidane A (2017) Multiscale damage evolution in polymer bonded sugar under dynamic loading. Mech Mater 114:97–106. https://doi.org/10.1016/j.mechmat.2017.07.016
24. Marchand A, Duffy J (1988) An experimental study of the formation process of adiabatic shear bands in a structural steel. J Mech Phys Solids 36(3):251–283. https://doi.org/10.1016/0022-5096(88)90012-9
25. Field JE (1992) Hot spot ignition mechanisms for explosives. Acc Chem Res 25(11):489–496. https://doi.org/10.1021/ar00023a002
26. Zhou M, Rosakis AJ, Ravichandran G (1996) Dynamically propagating shear bands in impact-loaded prenotched plates—I. Experimental investigations of temperature signatures and propagation speed. J Mech Phys Solids 44(6):981–1006. https://doi.org/10.1016/0022-5096(96)00003-8
27. Zhou M, Ravichandran G, Rosakis AJ (1996) Dynamically propagating shear bands in impact-loaded prenotched plates—II. Numerical simulations. J Mech Phys Solids 44(6):1007–1032. https://doi.org/10.1016/0022-5096(96)00004-X
28. Keyhani A, Yang R, Zhou M (2019) Novel capability for microscale in-situ imaging of temperature and deformation fields under dynamic loading. Exp Mech 59(5):775–790. https://doi.org/10.1007/s11340-019-00495-2
29. Hong SY, Kim YC, Wang M, Kim H-I, Byun D-Y, Nam J-D, Chou T-W, Ajayan PM, Ci L, Suhr J (2018) Experimental investigation of mechanical properties of UV-Curable 3D printing materials. Polymer 145:88–94. https://doi.org/10.1016/j.polymer.2018.04.067
30. Arruda EM, Boyce MC (1993) A three-dimensional constitutive model for the large stretch behavior of rubber elastic materials. J Mech Phys Solids 41(2):389–412. https://doi.org/10.1016/0022-5096(93)90013-6
31. Arruda EM, Boyce MC (1993) Evolution of plastic anisotropy in amorphous polymers during finite straining. Int J Plast 9(6):697–720. https://doi.org/10.1016/0749-6419(93)90034-N
32. Zhang P, To AC (2016) Transversely isotropic hyperelastic-viscoplastic model for glassy polymers with application to additive manufactured photopolymers. Int J Plast 80:56–74. https://doi.org/10.1016/j.ijplas.2015.12.012
33. Pan B, Qian K, Xie H, Asundi A (2009) Two-dimensional digital image correlation for in-plane displacement and strain measurement: a review. Meas Sci Technol 20(6):062001. https://doi.org/10.1088/0957-0233/20/6/062001
34. Blaber J, Adair B, Antoniou A (2015) Ncorr: open-source 2D digital image correlation matlab software. Exp Mech 55(6):1105–1122. https://doi.org/10.1007/s11340-015-0009-1
35. Sutton MA, Orteu JJ, Schreier H (2009) Image correlation for shape, motion and deformation measurements: basic concepts, theory and applications. 1 edn. Springer, United States. https://doi.org/https://doi.org/10.1007/978-0-387-78747-3
36. Wagner KB, Keyhani A, Boddorff AK, Kennedy G, Montaigne D, Jensen B, Beason M, Zhou M, Thadhani NN (2020) High-speed X-ray phase contrast imaging and digital image correlation analysis of microscale shock response of an additively manufactured energetic material simulant. J Appl Phys 127:235902. https://doi.org/10.1063/5.0003525
37. Seltzer R, Cisilino AP, Frontini PM, Mai Y-W (2011) Determination of the Drucker–Prager parameters of polymers exhibiting pressure-sensitive plastic behaviour by depth-sensing indentation. Int J Mech Sci 53(6):471–478. https://doi.org/10.1016/j.ijmecsci.2011.04.002
38. Dickson P, Parker G, Smilowitz L, Zucker J, Asay B (2006) Frictional heating and ignition of energetic materials. AIP Conf Proc 845:1057–1060. https://doi.org/10.1063/1.2263504